Batteries www.advenergymat.de

# The Impact of Initial SEI Formation Conditions on Strain-Induced Capacity Losses in Silicon Electrodes

Wei Zhang, Truong H. Cai, and Brian W. Sheldon\*

The solid electrolyte interphase (SEI) that passivates silicon surfaces in Li ion batteries is subjected to extremely large mechanical strains during electrochemical cycling. The resulting degradation of these SEI films is a critical problem that limits the cycle life of silicon-based electrodes. With the complex multiphase microstructure in conventional porous electrodes, it is not possible to directly measure the impact of these strains on SEI formation and capacity loss. To overcome this limitation a new in situ method is presented for applying controlled mechanical strains to SEI during electrochemical cycling. This approach uses patterned silicon films with different sized islands that act as model electrode particles. During lithiation/delithiation, the lateral expansion/contraction of the island edges applies in plane strains to the SEI. Detailed analysis of the island size effect then provides quantitative measurements of the impact of strain on the excess capacity losses that occur in different potential ranges. One key finding is that the applied strains lead to large capacity losses during lithiation only (during all cycles). Also, employing fast and slow SEI formation (first cycle) leads to large differences in the straininduced losses that occur during subsequent cycling.

#### 1. Introduction

Silicon (Si) is a promising anode material for lithium-ion batteries (LIBs), primarily because it has almost ten times larger capacity than the graphite that is widely used in commercial applications. [1–8] This high capacity is also accompanied by a large volume change (>300%), which leads to substantial mechanical degradation during repeated expansion and contraction of the electrode. The solid electrolyte interphase (SEI) layer is particularly vulnerable to damage, and this is widely recognized as one of the primary causes for the short cycle life of Si-containing LIBs. [9–12]

It is well established that the reduction of carbonate and other electrolytes forms SEI films on negative electrodes.<sup>[13–16]</sup> There is an extensive literature on the SEI that forms on a number of electrode materials, including silicon.<sup>[17–23]</sup> Substantial efforts have been made to improve the stability and performance of SEI, and detailed studies have characterized SEI films.<sup>[24–30]</sup> The latter have primarily addressed reaction chemistry, along with SEI

Dr. W. Zhang, T. H. Cai, Prof. B. W. Sheldon School of Engineering Brown University Providence, RI 02912, USA E-mail: brian\_sheldon@brown.edu

The ORCID identification number(s) for the author(s) of this article can be found under https://doi.org/10.1002/aenm.201803066.

DOI: 10.1002/aenm.201803066

composition and structure. The complex microstructure of most practical battery electrodes makes it extremely difficult to probe the mechanical deformation and degradation of SEI films. Thin-film electrodes have been employed to measure the elastic modulus of SEI layers.[31] However, in basic silicon thin films, the large volume changes during lithiation occur primarily in the "out-of-plane" direction, which does not produce the large lateral strains in the SEI layer that occur in most practical electrodes. To address this shortcoming, we previously reported experiments that employ patterned silicon islands instead of silicon films.[32,33] In that work, in situ atomic force microscopy (AFM) was then employed to monitor the effects of lateral strains that occur in the SEI that forms near the free edges of the islands. Herein, more accurate electrochemical measurements were employed with patterned silicon films, to provide direct quantitative

information about the impact of mechanical strains on SEI degradation and capacity loss during lithiation/delithiation cycles. A key feature of this novel approach is that there are no inactive components such as carbon black or binder in the electrodes, such that the measurements can directly track capacity losses due to degradation and other changes in the SEI films.

The methodology presented in this paper is based on using different sized silicon islands. Detailed analysis of these measurements provides a direct, quantitative value for the enhanced capacity losses due to strain. By making comparisons between strain-induced losses in these patterned and continuous silicon films where the SEI is not subjected strain, it was possible to show that the excess capacity losses to strain occur during lithiation, rather than delithiation. Mechanisms that can explain this effect are presented. The initial SEI structure was also varied by altering the first electrochemical cycle, where SEI films that were initially formed at slower rates led to significantly larger strain-induced capacity losses in subsequent cycles.

### 2. Results

## 2.1. Electrochemical Cycling of Patterned Silicon Islands

The SEI is largely created during the first cycle.<sup>[24,34,35]</sup> With this in mind, three different initial SEI's were created with the following procedures:

www.advenergymat.de

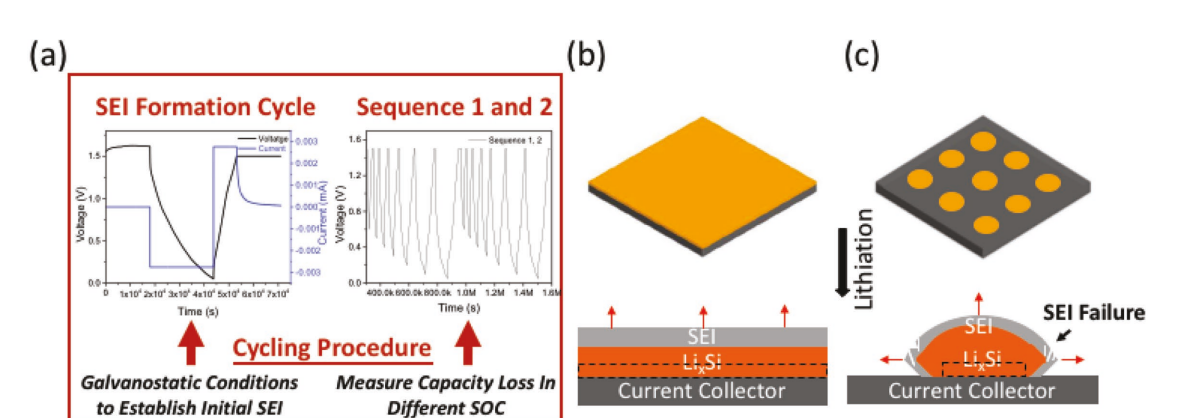


Figure 1. a) Different first cycles were used to vary SEI formation (slow cycle described in the text is shown here). Sequences of seven galvanostatic cycles were used to monitor capacity loss. b) Schematics of Si expansion for continuous films. c) Schematics of Si expansion with patterned Si islands. The dashed lines in (b) and (c) outline the size of the initial unlithiated silicon.

- Slow galvanostatic formation cycle: C/20 to 0.05 V; C/20 from 0.05 to 1.5 V.
- Fast galvanostatic formation cycle: C/2 to 0.05 V; C/2 from 0.05 to 1.5 V.
- Fast formation cycle with low voltage potentiostatic hold: C/2 to 0.05 V, hold at 0.05 V, and C/2 from 0.05 to 1.5 V. The duration of the potentiostatic hold was set such that the combined time for the C/2 portion and the hold was the same as the time used for the initial C/20 portion of the slow formation cycle.

Measurements after the SEI formation cycle were then used to obtain the irreversible capacities that are the focus of this investigation. As seen in Figure 1a, each sequence consisted of seven symmetric galvanostatic discharge-charge steps run at C/20 to progressively lower potentials (0.6, 0.5, 0.4, 0.3, 0.2, 0.1, 0.05 V). Thus, at the end of two of these sequences, the films were subjected to 15 discharge-charge cycles. The capacity loss measured during a symmetric lithiation-delithiation cycle provides a direct measure of lithium that is not recovered. The cycling sequence that was employed is designed to provide insight into the dynamic behavior of strains in the SEI layer during repeated cycling. For a symmetric cycle run to a given voltage, the capacity loss reflects SEI formation over that entire voltage range. Running a subsequent cycle to a lower voltage then provides information on the additional SEI losses during the additional increment (i.e., by looking at the extra amount lost).

As outlined in Section 1, the work presented here is designed to measure the impact of SEI strain on irreversible lithium consumption. This is based on our prior work, which shows that these losses are larger in patterned silicon islands, due to the strains applied to the SEI near the island edges.<sup>[32,33]</sup> The deformation of these types of silicon islands has been studied previously.[32,33,36] Figure 1b,c shows schematics of continuous and patterned silicon films during lithiation. Lithium insertion into the Si is accompanied by a large volume expansion, which is constrained by the Cu substrate. This leads to large out-of-plane expansion and in-plane compressive stress in the silicon, but these changes do not subject the SEI to significant strains. For the patterned silicon islands, interfacial shear near the edges produces a shear lag zone (SLZ) that permits lateral extension parallel to the substrate surface. The expansion of the lithiated Si in the SLZ applies large in-plane strains to the SEI. Note that the center of the islands (outside of the SLZ) is similar to the continuous films, with large out-of-plane expansion (out-plane expansion in the SLZ is less extensive, but still significant).

To verify the lithiation induced changes that occur in the patterned films, samples before and after cycling were examined with scanning electron microscopy (FIB, FEI HELIOS 600). Figure 2 shows representative images of as-deposited silicon islands, along with similar islands after cycling. The initial islands here are circular with a diameter ≈19 µm (Figure 2a). After 14.5 cycles (after the last lithiation to 0.05 V), there is an obvious increase in diameter to ≈23 µm (Figure 2b). After 15 fully cycles (i.e., when the voltage is returned to 1.5 V), the

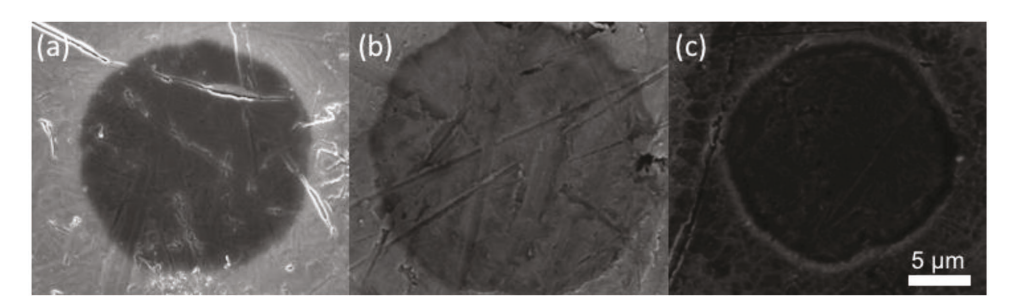


Figure 2. a) SEM images of patterned Si island before cycling. Similar samples with a "slow" SEI formation cycle: b) after 14.5 cycles (sequence 2, after final lithiation to 0.05 V; c) after 15 cycles (sequence 2, with delithiation back to 1.5 V).

ADVANCED ENERGY MATERIALS

island shows slight difference slight decrease compared to its original size ( $\approx$ 19  $\mu$ m).

#### 2.2. Capacity Measurements

As outlined in the previous section, the central idea we are using is that the patterned islands undergo expansion/contraction in the SLZ, which then produces large strains in the SEI. In previous work, the size of the SLZ was estimated with in situ AFM measurements.[33] However, the electrochemical data obtained with these in situ AFM cells are typically less precise than measurements using coin cells. Thus, to obtain more precise electrochemical information about the capacity losses in the SLZ, we are now using a different approach based on multiple island sizes. The rationale for this is that the mechanisms which dictate the SLZ should be the same in different sized islands. Thus, the size of the SLZ can be inferred by analyzing the response of different islands. Besides eliminating the need for in situ AFM measurements, we also believe that this approach provides more accurate information about strain-induced SEI losses, as a function of the SOC. The methodology we have developed to analyze these experiments is described in more detail in Section 3.

For the patterned films there are three contributions to the capacity losses due to SEI: in the SLZ (with lateral strain), in the center of the silicon islands (no lateral strain), and on the copper current collector between the islands. Thus, to obtain data on the influence of strains, capacity measurements were conducted with three types of films—continuous and patterned silicon and also on the Cu current collector. The first step in

evaluating the data is to subtract contributions from the copper, which requires measurements on copper electrodes tested with the same current densities as the corresponding patterned Si film (note that a different Cu measurement is then required for each island size). The relative area of the silicon ( $\alpha_0$ ) was obtained from SEM images of the patterned samples. Then, the specific gravimetric lithiation capacity ( $c_{P,gr}^{lith}$ , mAh  $g^{-1}$ ) from the Si part can be expressed as:

$$c_{P,gr}^{lith} = \frac{C_P^{lith} - (1 - \alpha_o) C_{Cu}^{lith}}{\alpha_o h_o A_{tot} \rho}$$
(1)

where  $C_{\rm P}^{\rm lith}$  and  $C_{\rm Cu}^{\rm lith}$  are measured capacities during the lithiation cycle only ( $\mu$ A h).  $\alpha_{\rm o}$ ,  $h_{\rm o}$ ,  $A_{\rm tot}$ , and  $\rho$  are the initial area fraction of Si in the patterned films, the Si film thickness, the total area of the substrate and the density of silicon. The delithiation capacity can be calculated with a similar approach.

The corrected lithiation and delithiation capacities for the data collected after the initial slow formation cycle are shown in Figure 3 (comparable results were also obtained for the other two formation cycles). The values here are reported as capacities per gram of the silicon. Two key trends are immediately obvious:

- During lithium removal the capacities are similar.
- The opposite occurs during lithium insertion, where capacity increases with decreasing island size, and the lowest capacities were observed in the continuous films.

For the continuous films, the coulombic efficiency is relatively high (>95%) and the measured initial discharge

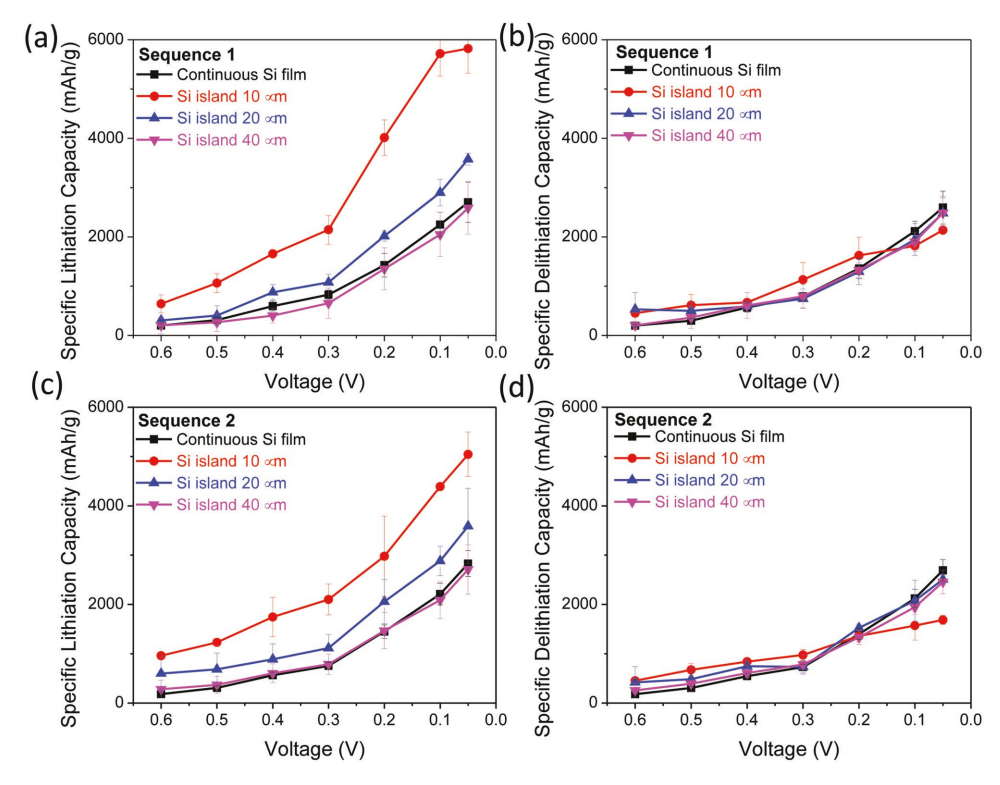


Figure 3. Capacities of Si islands (10, 20, and 40  $\mu$ m) during lithiation and delithiation for a,b) sequence 1; and c,d) 2 based on Equation (1). These results are obtained after the slow SEI formation cycle samples (C/20).



**Table 1.** Capacities of thin film samples (continuous silicon, patterned films) during the formation cycle.

Samples	Lithiation capacity	Delithiation capacity
Continuous Si film	$3330 \pm 690$	$2810 \pm 290$
Si island 10 μm	$7690 \pm 1690$	$2020\pm290$
Si island 20 μm	$5490 \pm 180$	$2020\pm200$
Si island 40 μm	$3890 \pm 1130$	$2410 \pm 260$

capacity (based on a film thickness of 50 nm film thickness) is  $\approx 3330$  mAh g<sup>-1</sup> (Table 1). This is reasonably close to the maximum Li capacity in silicon, which is consistent with prior work. [37,34] For the 40  $\mu$ m islands, the capacities are similar to the continuous films. As the island size decreases the lithiation capacities are noticeably higher while the delithiation capacities are slightly lower. A likely cause for the lower delithiation capacities is that the as-deposited islands are thinner near the edges due to shadowing effects. The much higher capacities (higher than the full capacity of pure silicon) measured during discharge indicate that more lithium ions are consumed during this part of the cycle (the majority of the losses due to SEI occur). This effect is evaluated in more detail in Section 3.

The irreversible capacity per Si is obtained directly from experimental values, via:

$$\frac{C_{\text{Si}}^{\text{irr}}(t_{\text{P}})}{A_{\text{Si}}} \cong \frac{C_{\text{P}}^{\text{irr}} - (1 - \alpha_{\text{o}}) C_{\text{Cu}}^{\text{irr}}(t_{\text{Cu}})}{\alpha_{\text{o}} A_{\text{tot}}}$$
(2)

where  $C_{\rm P}^{\rm irr}$  and  $C_{\rm Cu}^{\rm irr}$  are measured irreversible capacities for patterned and copper reference films, respectively ( $\mu$ A h).  $t_{\rm P}$  and  $t_{\rm Cu}$  are the duration of the galvanostatic cycles for patterned and reference films. Further interpretation of these values is presented in Section 3.

Figure 4a,b reports specific capacity losses for continuous Si film and samples with different island sizes (10, 20, and 40  $\mu$ m). For cycles run to 0.6, 0.5, and 0.4 V, the continuous Si films and patterned islands have small capacity losses, which are consistent with limited silicon lithiation (and hence minimal strain applied to the SEI). However, capacity losses in the patterned films increase sharply at lower potentials, where significant lithiation of the silicon leads directly to large lateral expansions/contractions in the SLZ. [32] These losses are larger in smaller islands, which is consistent with increased strain-induced losses in the SLZ (i.e., because a larger fraction of the silicon is in the SLZ with smaller islands).

Parallel measurements were also conducted with the faster formation cycles described in Section 2.1. These are reported in Figure 4c–f (without and with the low voltage potentiostatic hold. For the third formation cycle (Figure 4e,f), data were not collected for 40 µm patterned specimens. The other measurements show that these larger islands have only slightly higher capacity losses than the silicon continuous films (i.e., in Figure 4a–d). Therefore, the relative experimental error in these measurements was larger and the data were less useful for the quantitative analysis of strain effects. In comparison with the data in Figure 4a,b, the results in Figure 4c,d used a much shorter formation time. The experiments with the third formation cycle (Figure 4e,f) employ the same time as Figure 4c,d

for the initial cycling to 0.05 V, but with the subsequent potentiostatic hold the total time before the first delithiation is now similar to that used for the slow formation cycle. Thus, for the results in Figure 4e,f, the time for the initial formation cycle is similar to that for Figure 4a,b, but with much less time spent at higher potentials. It is important to keep in mind that all of the data in Figure 4 were obtained under identical cycling conditions, after these initial formation cycles. Thus, the differences between these results reflect the impact of the formation cycle on subsequent cycling behavior. The general trends in Figure 4c-f are similar to those in Figure 4a,b, with much higher losses at lower potentials and increasing loss with decreasing island sizes. The most notable difference is that the patterned films in both Figure 4c,d and Figure 4e,f show significantly smaller irreversible capacities than the corresponding samples in Figure 4a,b. This indicates that the faster formation cycle leads to less loss during subsequent cycling. The similarity between the results in Figures 4c,d and e,f indicates that the time spent at low potentials during SEI formation does not have a major effect. Instead, the primary cause of the decreased capacity losses in Figure 4c,d and Figure 4e,f appears to be the shorter exposure times at higher potentials (i.e., during the first galvanostatic discharge cycle). Additional discussion of these comparisons are presented in Section 3.

The results in Figure 4 are the primary data that are used for our analysis of SEI formation. Because these are obtained as a difference, they are not significantly impacted by the thickness effects described above. The observed increases in irreversible capacities with decreasing island size are consistent with the expectation that the SLZ occupies a larger fraction of the smaller islands. The detailed analysis described in Section 3 was then employed to account for the expansion of different sized islands. This makes it possible to distinguish the irreversible losses in the SLZ from the unstrained values obtained with continuous films.

## 2.3. Additional Characterization

Several other methods were employed to provide important additional information about the changes that occur during electrochemical cycling. The measurements in Figure 5 indicate that the SEI formed in the SLZ differs in composition from the SEI in the middle of the same island. Figure 5a shows locations where EDS point scans were conducted on a 20 µm patterned film after sequence 2 with a slow formation cycle. Here, several different points have been chosen from two regions: one close to the edge of the island and one in the center region of the island. Strict quantitative interpretation of the F and O signals is not possible, however, the F/Si and O/Si intensity ratios are plotted in Figure 5b. These results indicate that higher F and O intensities occur near the edge region. This is consistent with composition analysis in our prior work, where detailed TOF-SIMS profiling indicated that LiF and Li<sub>2</sub>CO<sub>3</sub> were more prevalent in SEI films on patterned silicon islands.[32] The enhanced fluorine and oxygen signals in Figure 5b are thus likely to be caused by more LiF and Li<sub>2</sub>CO<sub>3</sub> (or possibly more Li<sub>2</sub>O) in the SLZ. These higher F and O levels match our previous work, and reflect more SEI film formation in the shear



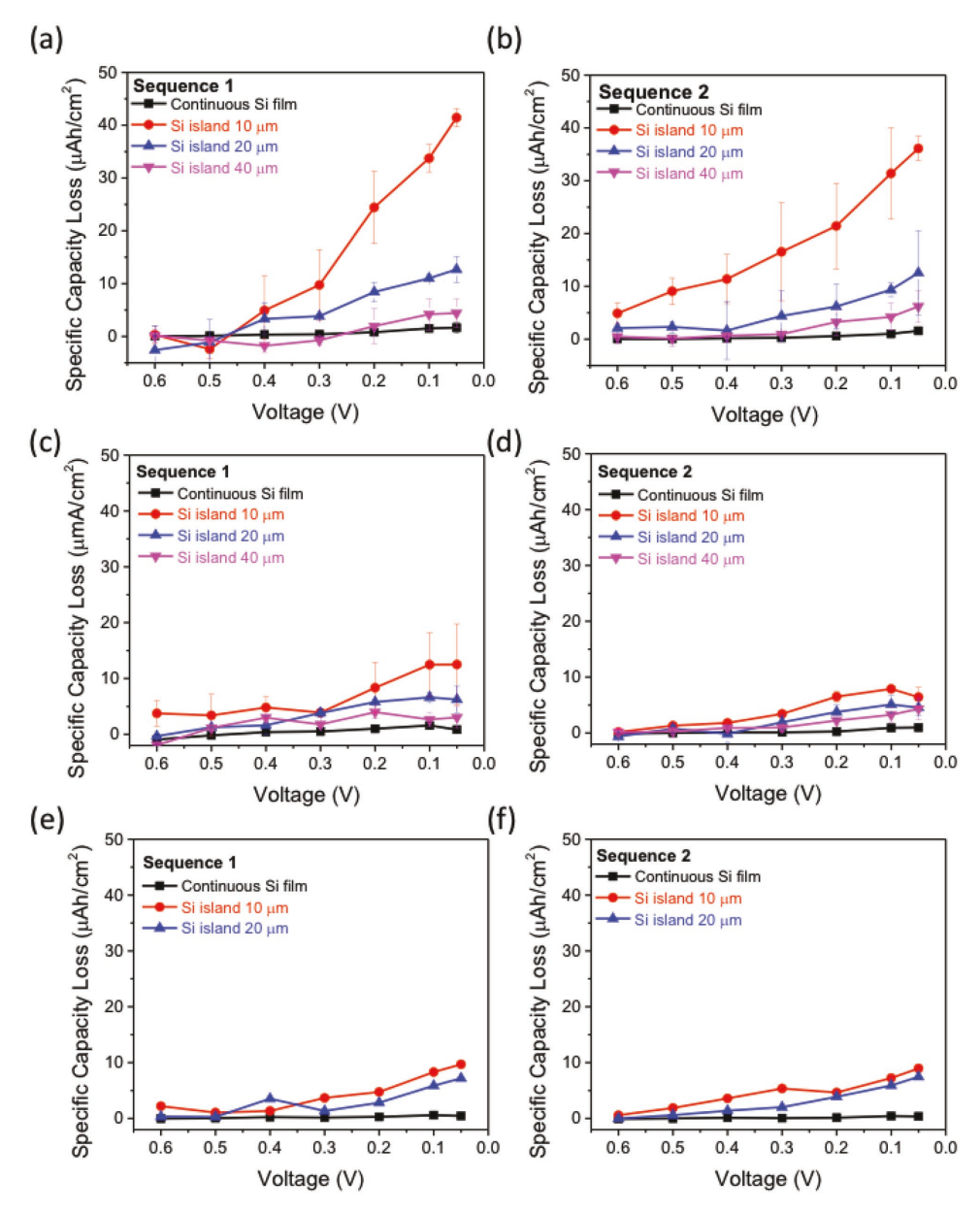


Figure 4. Irreversible capacities of continuous and patterned silicon films during sequence 1 and sequence 2 with different formation cycles: a,b) slow formation cycle (C/20); c,d) fast formation cycle (C/2); e,f) a fast formation cycle (C/2) and a voltage hold at 50 mV. The voltage hold was added so that the total time for this formation cycle was the same as that in the slow formation cycle used for (a) and (b).

lag zone. To further support this, EDS line scans across islands were also performed. In Figure 5c the Si, O, and F signals are only observed in the island region (blue, green, and red curves), whereas the higher intensity Cu peaks from the current collector that are observed everywhere (violet curve). The scan for F in Figure 5d is symmetric, with relatively constant intensity in the middle region (light green shading), which corresponds to the inner area where there is no lateral strain applied to the SEI. The measured size of this region is  $\approx 11.4 \pm 1.2 \ \mu m$ , which is significantly smaller than the initial diameter of these islands ( $\approx 19 \ \mu m$  by SEM). Based on these values, the approximate size of the SLZ is 3.8  $\pm$  0.6  $\mu m$ ). Additional analysis related to the size of the SLZ during cycling is discussed in Section 3.

Cross-sectional images from FIB cut 20  $\mu m$  islands were used to measure electrode thicknesses after full delithiation. Figure S1 (Supporting Information) shows a typical image of a cycled electrode. As seen here, a clear planar boundary is visible between the silicon and the SEI film. The Cu current collector layer, silicon, and SEI are all identified (a Pt coating layer is on the top used to protect the samples from the Ga+ ion cutting). The Si thickness after delithiation is 67 nm, which is larger than its original size (50 nm) due to the irreversible volume change during cycling. Multiple measurements of this type were obtained from FIB cross-sections (for consistency, only images near the island centers were used for these measurements). The average SEI thickness obtained at the end of

www.advenergymat.de

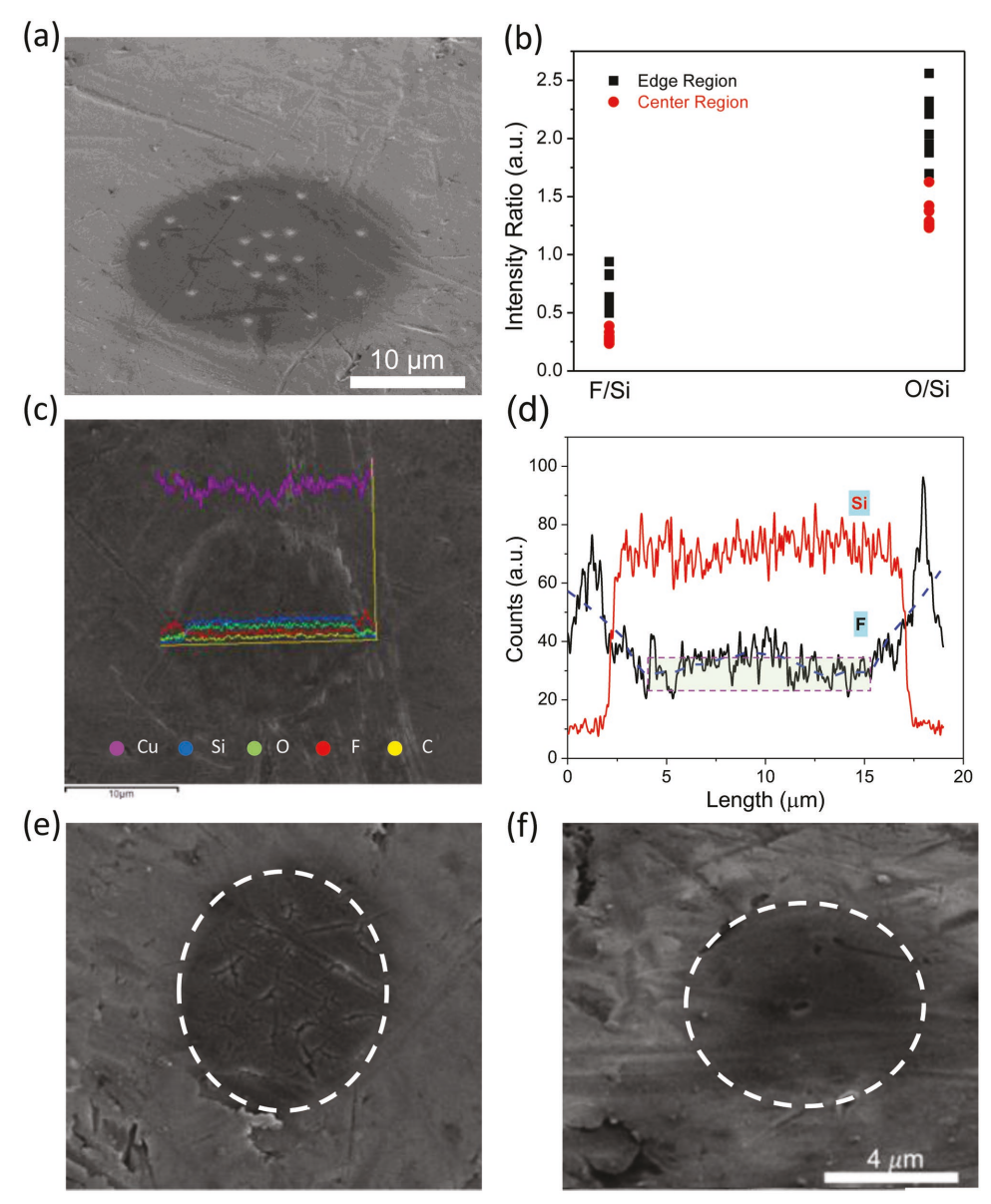


Figure 5. a) The position of EDS point scans in a 20  $\mu$ m patterned island after sequence 2 with a slow formation cycle. b) The intensity ratios of F/Si and O/Si for these point scans. c) EDS line scans across a randomly chosen island from the same sample. d) Spectra of elements Si and F. The distribution of F is not uniform in the whole island. The middle shadow region shows a relatively similar intensity indicating the size of the non-sliding zone. SEM images of Si island (10  $\mu$ m) after 15 cycles (end of sequence 2), where different initial SEI formation cycles were used: e) C/20 and f) C/2.

Sequence 2 was  $56 \pm 13$  nm when the C/20 formation cycle was used,  $35 \pm 9$  nm when the C/2 formation cycle was used, and  $38 \pm 12$  nm for the C/2 formation cycle with the low potential hold These values are comparable to other reported values for silicon electrodes. [10,31] The thinner layer observed with a faster formation cycle is consistent with the trend observed in our prior AFM study of SEI growth. [39] The initial SEI thickness is primarily established by organic components (mainly carbonrich electrolyte decomposition products) at higher potential (0.3–1.2 V), and the inorganic constituents (i.e., Li<sub>2</sub>CO<sub>3</sub>, Li<sub>2</sub>O, LiF) are then formed at lower potential ( $\le 0.3$  V). [39] Thus a slower initial rate (C/20 here) leads to the formation of more organic components and thicker SEI at higher potentials. The idea that the initial thickness is largely determined by the rate

used in the formation cycle is also consistent with the similar thicknesses observed using C/2 formation cycles with and without the 0.05 V hold.

The SEM images in Figure 5e were taken at the end of sequence 2 (i.e., after 15 total cycles). When the slow formation cycle was used, there are numerous cracks on the surface, whereas these cracks are seldom seen when the fast formation cycle was used (Figure 5f). These observations are consistent with several previous in situ AFM investigations using similar Si islands, where: 1) cracking in the SEI occurred in relatively thick SEI layers,<sup>[33]</sup> and 2) a short exposure time at higher potentials (faster SEI formation cycle) produces thinner SEI.<sup>[39]</sup> Based on these combined observations, it appears that the C/20 formation cycle produced thicker SEI that is more susceptible

ADVANCED ENERGY MATERIALS

to cracking during Sequences 1 and 2. The cracking here also appears to be correlated with the higher capacity losses (i.e.,  $C_{\rm Si}^{\rm irr}$ ) measured when the slow formation cycle was used (see Section 2.2).

To obtain addition information about the impact of the C/20 and C/2 formation cycles, EIS was performed on continuous silicon films (interpretation of EIS spectra is more difficult in patterned films, because of contributions from both the Cu and Si surfaces).<sup>[32]</sup> As shown in Figure S2a (Supporting Information), the spectra exhibit one broad semicircle that is attributed to an overall interfacial resistance (including charge transfer). Variations in this resistance during sequence 1 and 2 cycling are reported in Figure S2(b) (Supporting Information). The slow formation cycle leads to lower interfacial resistance initially, but higher interfacial resistance in all subsequent cycles. This is consistent with EIS results obtained in our prior work where fast initial cycling reduced the SEI thickness and the interfacial impedance (with a different electrolyte).[39] All of these results clearly confirm that variations in the initial formation cycle lead to different SEI behavior that persists throughout our experiments.

## 3. Analysis

#### 3.1. Impact of Island Size

Quantitative analysis of the results in section 2 is primarily based on comparing capacity losses with different sized islands to those in continuous silicon films. The value of  $C_{\rm Si}^{\rm irr}$  in Equation (2) can be further interpreted by describing the irreversible lithium losses during both parts of the cycle with averaged current densities  $\langle i_{\rm lith}^{\rm irr} \rangle$  and  $\langle i_{\rm del}^{\rm irr} \rangle$ 

$$C_{\text{Si}}^{\text{irr}} = A_{\text{tot}} \left( \left\langle i_{\text{lith}}^{\text{irr}} \right\rangle t_{\text{lith}} + \left\langle i_{\text{deli}}^{\text{irr}} \right\rangle t_{\text{deli}} \right) \tag{3}$$

These two average values cannot be independently determined from just the measurements on a patterned film. However, for the continuous silicon thin films we assume that the following approximation can be used for data that is collected after the formation cycle

$$\left\langle i_{\mathrm{lith},\infty}^{\mathrm{irr}} \right\rangle \cong \left\langle i_{\mathrm{deli},\infty}^{\mathrm{irr}} \right\rangle \cong \left\langle i_{\infty}^{\mathrm{irr}} \right\rangle = \frac{I_{\infty} \left( t_{\mathrm{lith},\infty} - t_{\mathrm{deli},\infty} \right)}{A_{\mathrm{tot}} \left( t_{\mathrm{lith},\infty} + t_{\mathrm{deli},\infty} \right)} \tag{4}$$

where  $I_{\infty}$  is the current and  $t_{\mathrm{lith},\infty}$  and  $t_{\mathrm{deli},\infty}$  are the measured times for the experiments on continuous films. The equivalence in Equation (4) is not expected to hold in the first cycle, where most of the SEI initially forms during lithiation. However, after the SEI is in place the average current densities during the two halves of the cycle are likely to be roughly similar for the continuous films where there is no strain applied to the SEI, and the current and the area are both fixed. This is consistent with the low capacity losses in the continuous films, and thus  $\langle i_{\infty}^{\mathrm{irr}} \rangle$  is an appropriate reference value that can be compared to the results obtained with patterned films.

The strains applied to the SEI in the SLZ were estimated by describing the expansion and contraction that occurs in the underlying silicon. The change in the electrode volume as a function of the lithium content is given by

$$V(\chi) = V_{\rm m}^{\circ} + \int_{0}^{x} \overline{V_{\rm Li}} \, d\chi \cong V_{\rm m}^{\circ} + \overline{V_{\rm Li}} \, \chi \tag{5}$$

where  $\chi$  is the molar lithium to silicon ratio,  $V_{\rm m}^{\rm o}$  is the molar volume of pure Si, and  $\overline{V_{\rm li}}$  is the partial mole of lithium in the alloy. The approximation on the far right assumes that  $\overline{V_{\rm li}}$  is constant with respect to changes in composition. If the expansion is isotropic, the linear expansion strain due to lithiation, f, is given by

$$f = \left[1 + \frac{\overline{V_{\text{Li}}} \chi}{V_{\text{m}}^{\circ}}\right]^{\frac{1}{3}} - 1 \tag{6}$$

The expansion of an  $\mathrm{SiLi}_\chi$  island can be described as a function of f. It is convenient to start with the previously published elastic model of the SLZ in circular islands.<sup>[40]</sup> This description, summarized in Appendix A, divides the islands into two zones:

Inner Region ( $0 \le r \le R_p$ ): The electrode material behaves like a continuous Si film (i.e.,  $u(r,\chi)=0$ ). Here, the volume expansion that occurs during lithiation leads to uniform, in-plane stresses.

Outer Region ( $R_P \le r \le R$ ): The electrode material is in the SLZ, where the volume changes in the lithiated silicon push the material outward (in the r direction), against the shear resistance,  $\tau_s$ , at the interface. The reverse process occurs during delithiation. When the initial island size  $R_o$  and  $\chi$  are specified, values of  $R_p(\chi)$  and  $R(\chi)$  can be obtained from the analysis in the Appendix. In the SLZ the surface area increases and corresponding in-plane strains that occur in the silicon apply strain to the SEI that is on the top of the islands. The size of the SLZ is  $S = R - R_p$ , which then gives

$$\alpha_{\rm S}(R, R_{\rm P}) \cong \left(\frac{R}{R_{\rm o}}\right)^2 - \left(\frac{R_{\rm p}}{R_{\rm o}}\right)^2 \cong \frac{2 S R - S^2}{R_{\rm o}^2} \tag{7}$$

The elastic analysis (see Appendix) is only fully valid at relatively low values of  $\chi$ . After the in-plane stress in the center of the island,  $\sigma_{\rm el}^{\infty}$ , reaches the yield stress,  $\sigma_{\rm f}^{*}$ , the deformation of the island is more complex. The elastic analysis is thus limited to a maximum composition of  $\chi = \chi^{*}$ , which can be described by rearranging Equation (A6) to give

$$\chi^* \cong -\frac{3 V_{\rm m}^{\circ}}{\overline{V_{\rm ti}}} \left(\frac{1 - \nu_{\rm f}}{E_{\rm f}}\right)^* \sigma_{\rm f}^* = -\frac{3 V_{\rm m}^{\circ}}{\overline{V_{\rm ti}}} \varepsilon^* \tag{8}$$

Reasonable estimates for the quantities on the right-hand side are available (see Table S1, Supporting Information). These give  $\chi^* \cong 0.4$ . The solution in Equations (A4)–(A7) can then be used to obtain the dimensions  $R_p^*$  and  $R^*$ , for given values of the initial island dimensions ( $h_o$  and  $R_o$ ), and the interfacial shear resistance  $\tau_s$ . This elastic analysis is based on small strain, which is generally valid up to the small  $\chi^*$ . For  $\chi > \chi^*$ , the inner region undergoes plastic flow. The relatively small value of  $\chi^*$  implies that this condition is prevalent for most of the lithiation (and delithiation) process. This also means that lateral strains in the SLZ are small for  $\chi < \chi^*$ , such that most of the excess capacity loss due to strain occurs for  $\chi > \chi^*$ .

MATERIALS
www.advenergymat.de

The data reported in Figure 4 clearly show an increase in irreversible capacity with small islands. These measurements make it possible to evaluate the excess Li loss due to strain in the SLZ. The measured irreversible capacities for the patterned films (see Equation (2)) can be subdivided into contributions from the exposed copper current collector, the silicon inner region (no lateral strain), and the SLZ:

$$C_{\mathrm{P}}^{\mathrm{irr}}\left(t_{\mathrm{P}}\right) = A_{\mathrm{tot}} \left[ \left(1 - \alpha_{\mathrm{o}}\right) \int_{0}^{t_{\mathrm{P}}} i_{\mathrm{Cu}}^{\mathrm{irr}} \, \mathrm{d}t + \alpha_{\mathrm{o}} \left( \int_{0}^{t_{\mathrm{P}}} \left(1 - \alpha_{\mathrm{S}}^{*}\right) i_{\mathrm{o}}^{\mathrm{irr}} \, \mathrm{d}t + \int_{0}^{t_{\mathrm{P}}} \alpha_{\mathrm{S}}^{*} \, i_{\mathrm{SLZ}}^{*} \, \mathrm{d}t \right) \right] \quad (9)$$

where  $\alpha_s^*$  is the relative area of the SLZ at the onset of plastic flow, which is given by Equation (7) with  $S = S^*$ .

In Equation (9),  $i_{\rm SIZ}^*$  is the irreversible current density per area of the Si that is initially in the SLZ (the increase in the actual SLZ area as a function of  $\chi$  is then considered further below). It is convenient to redefine  $i_{\rm SLZ}^* = i_{\infty}^{\rm irr} + \Delta i_{\rm SLZ}^*$  to obtain:

$$\alpha_{\rm S}^* \int_0^{t_{\rm V}} i_{\rm SLZ}^* \, \mathrm{d}t = \alpha_{\rm S}^* \int_0^{t_{\rm V}} i_{\infty}^{\rm int} \, \mathrm{d}t + \alpha_{\rm S}^* \int_0^{t_{\rm V}} \Delta i_{\rm SLZ}^* \, \mathrm{d}t \tag{10}$$

Noting that  $\alpha_s^*$  is a fixed value and inserting this in Equation (9) then leads to

$$\Delta \kappa_{\rm S} \equiv \frac{\left\langle \Delta i_{\rm SLZ}^{\star} \right\rangle}{\left\langle i_{\infty}^{\rm irr} \right\rangle} = \frac{1}{\left\langle i_{\infty}^{\rm irr} \right\rangle t_{\rm p}} \int_{0}^{t_{\rm p}} i_{\rm SLZ}^{\rm irr} \, dt$$

$$\equiv \frac{1}{\left(2\lambda^{\star} + \lambda^{\star 2}\right)} \left[ \frac{C_{\rm p}^{\rm irr} \left(t_{\rm p}\right)}{A_{\rm tot} \, \alpha_{\rm o} \left\langle i_{\infty}^{\rm irr} \right\rangle t_{\rm p}} - \frac{(1 - \alpha_{\rm o}) \left\langle i_{\rm cu}^{\rm irr} \right\rangle}{\alpha_{\rm o} \left\langle i_{\infty}^{\rm irr} \right\rangle} - 1 \right] \tag{11}$$

where  $\lambda^* = \frac{S^*}{R_o}$ . The value of  $\langle \Delta i_{SLZ}^* \rangle$  is a measure of the excess capacity loss due to strain in the SEI. This form is convenient because  $\langle \Delta i_{SLZ}^* \rangle$  can be calculated directly from experimentally determined quantities if  $S^*$  is known (i.e., the other quantities on the far right side of Equation (11) are obtained directly from the experiments described in Section 2).

## 3.2. Strain-Induced Capacity Loss

Quantitative interpretation of the experiments is largely focused on the value of  $\langle \Delta i^*_{SIZ} \rangle$  that is obtained with Equation (11), and thus it is important to consider this quantity more carefully. The values of  $\langle i^{\rm ir}_{\rm Cu} \rangle$  and  $\langle i^{\rm ir}_{\infty} \rangle$  reflect averages over the state of charge during galvanostatic cycling. This is also the case for  $\langle \Delta i^*_{SIZ} \rangle$ , but in the SLZ there are also significant spatial variations (at a given  $\chi$ ) that do not occur in the continuous film reference measurements. The values of  $\langle \Delta i^*_{SIZ} \rangle$  are the capacity losses that are induced by the average strain field in the SLZ. Here, it is convenient to summarize the impact of the overall strain distributions in terms of the relative, average area of the material that is in the SLZ:

$$\frac{\alpha_{\rm S}^* + \Delta \alpha_{\rm S}(\chi, R_{\rm o}, S)}{\alpha_{\rm S}^*} = \frac{R(\chi)^2 - R_{\rm P}^{*2}}{R_{\rm o}^2 - R_{\rm P}^{*2}} = \frac{R_{\rm P}^{*2}(p^2 - 1) + 2R_{\rm P}^*pS + S^2}{2S^*R_{\rm P}^* + S^{*2}}$$
(12)

where  $p(\chi) = \frac{R_p(\chi)}{R_p^*}$  (see Appendix). If *S* is a fixed value (i.e.,  $S = S^*$ ), this simplifies to

$$\frac{\Delta \alpha_{\rm S}(\chi, R_{\rm o}, S)}{\alpha_{\rm S}^*} = \frac{R_{\rm p}^*}{S^*} \frac{R_{\rm p}^*(p^2 - 1) + 2S^*(p - 1)}{2R_{\rm p}^* + S^*} \\
= \frac{(1 - \lambda^*)^2 (p^2 - 1)}{2\lambda^* - \lambda^{*2}} + \frac{2(1 - \lambda^*)(p - 1)}{(2 - \lambda^*)} \tag{13}$$

This quantity varies only slightly with  $R_o$  (on the order of a few percent in our analysis). Thus, while the relative size of the SLZ (i.e.,  $\alpha_S$ ) is larger in smaller islands, the average strain in the SLZ (i.e., approximated with  $\Delta\alpha_S$ ) is not a strong function of  $R_o$ .

The analysis method that we employed uses data from different sized islands to obtain a self-consistent value of  $\hat{s}^*$ . As outlined in the Appendix, values of S are closely related to but not identical to  $\hat{s}$ . The latter is defined by several key physical properties (see Equation (A8)), whereas S is weakly dependent on  $R_0$ . At the onset of plastic flow

$$\hat{\mathbf{s}}^* = -\frac{\left(\sigma_{\text{el}}^{\infty} h\right)^*}{\tau_{\text{s}}^*} \tag{14}$$

For films that match our experiments, values of  $(\sigma_{\rm sl}^{-a}h)^*$  have been measured directly. [41,42] Thus,  $\tau_{\rm s}$ \* is the key unknown quantity that determines  $\hat{s}^*$  (and hence  $S^*$ ). In the limit of small  $\hat{s}^*$  (i.e.,  $\hat{s}^* \ll R_{\rm o}$ ),  $S^* \cong \hat{s}^*$  and data for different  $R_{\rm o}$  can be fit directly to Equation (10) to obtain values of  $\hat{s}^*$  and  $\Delta i_{\rm SLZ}^*$ ). This approach was modified for our experiments, where the size of the SLZ does not satisfy the  $\hat{s}^* \ll R_{\rm o}$  criteria. Under these conditions, the value of  $S^*$  for a given  $\hat{s}^*$  and  $R_{\rm o}$  can be obtained from Equations (A6) to (A8). The experiments were fit to data for different sized islands to obtain  $\hat{s}^*$ , and this value was then used to obtain  $\Delta i_{\rm SLZ}^*$  as a function of  $\Delta i_{\rm SLZ}^*$  (the key relationship we are interested in). For each cycle, the experimental measurements give

$$\frac{\langle \Delta \alpha_{\rm S} \rangle}{\alpha_{\rm s}^*} = \frac{\int_0^{t_{\rm inh}} \Delta \alpha_{\rm S} \, \mathrm{d}t}{\alpha_{\rm s}^* t_{\rm bish}} = \frac{\left(1 - \lambda^*\right)}{t_{\rm bish} \left(2 - \lambda^*\right)} \int_0^{t_{\rm p}} \left(\frac{\left(1 - \lambda^*\right)}{\lambda^*} \left(p^2 - 1\right) + 2\left(p - 1\right)\right) \, \mathrm{d}t \quad (15)$$

As noted above, this value should exhibit only small variations with  $R_0$ .

The methodology described above was employed to analyze the experimental results in Section 2. Values for  $\Delta\kappa_S$  are plotted in **Figures 6** and 7, for the slow (C/20) and fast (C/2) formation cycles respectively (the cycles run to 0.6 and 0.5 V are not included, since most of the silicon lithiation occurs at lower potentials). The best fit was obtained for a value of  $\hat{s}^*=3.1~\mu m$ . This value is also comparable to the size of the shear lag zone obtained from the composition profiles in Figure 4. This provides important validation of our method, since it indicates that the estimated size of the SLZ obtained from only the electrochemical data (i.e.,  $\hat{s}^*$ ) is accurate.

Each point in Figures 6 and 7 is based on one of the full cycles during Sequence 1 or 2. This comparison shows very good agreement between the results obtained with the 10 and 20  $\mu m$  islands. The 40  $\mu m$  island results are somewhat more scattered, which is not surprising since the difference between the data obtained with patterned and continuous films was significantly smaller. However, most of the data for the 40  $\mu m$  islands is roughly consistent with results for the smaller islands.

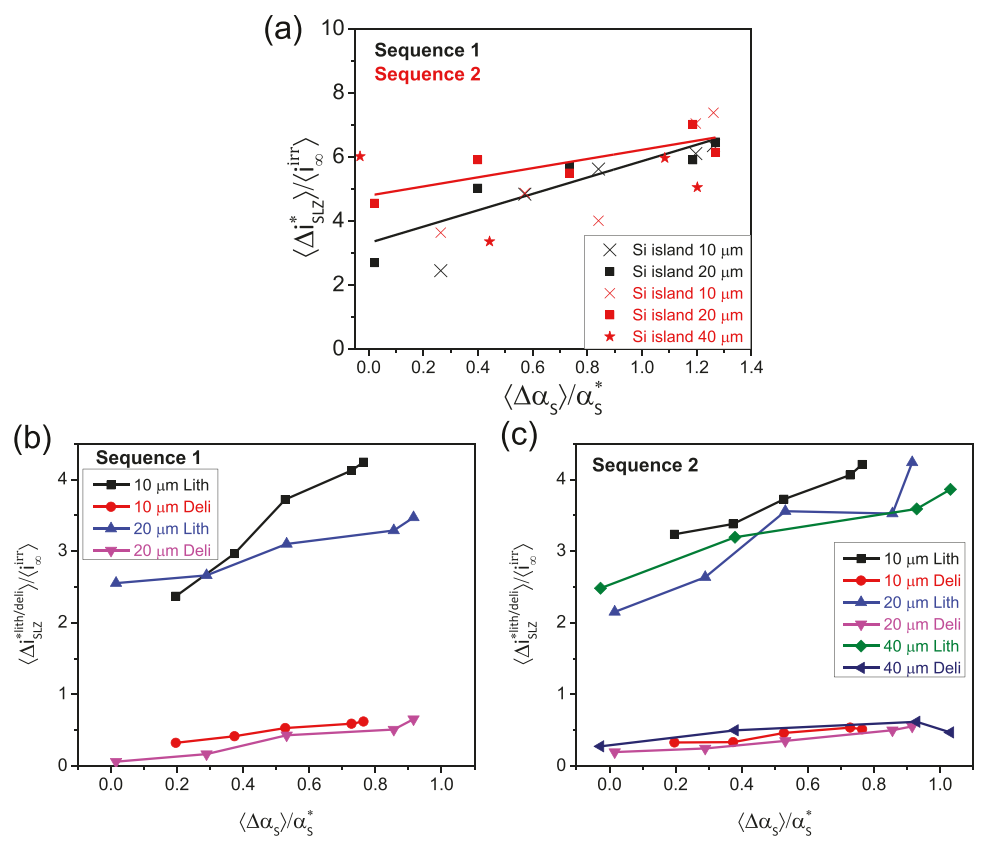


Figure 6. Relative capacity loss due to strain in the shear lag zone, for SEI created with the slow formation cycle (C/20). a) Overall losses, based on applying Equation (11) to the data in Figure 3. The black line is fit to all of the Sequence 1 values (i.e., for different island sizes) and the red line is fit to all of the Sequence 2 values. b) Strain induced losses during lithiation and delithiation for Sequence 1, based on Equations (19) and (22). c) Strain induced losses for Sequence 2.

All of the results in Figures 6a and 7a show that  $\Delta \kappa_s$  (the excess irreversible current-density ratio in the SLZ) becomes progressively larger when the cycle depth moves to lower potentials. This coincides with the increasing volume expansion of the silicon which occurs at these potentials.

If the values of  $\langle i_{C_{11}}^{irr} \rangle$  and  $\langle i_{\infty}^{irr} \rangle$  are assumed to be the same during the lithiation and delithiation portions of each cycle, then the capacity losses in the SLZ during the two parts of the cycle can be separated. For the lithiation portion, the full measured capacity of the electrode is given by

$$C_{P}^{\text{lith}}\left(t_{\text{lith}}\right) = A_{\text{tot}}\left[\alpha_{o}\left(\int_{0}^{t_{\text{lath}}}i_{\infty}dt + \alpha_{s}^{*}\int_{0}^{t_{\text{lith}}}\Delta i_{\text{SLZ}}^{*}dt\right) + (1-\alpha_{o})\int_{0}^{t_{\text{lith}}}i_{\text{Cu}}dt\right] \quad (16)$$

The contribution from unstrained Si can be broken into reversible and irreversible contributions  $(i_{\infty} = i_{\infty}^{\text{rev}} + i_{\infty}^{\text{irr}})$ . These are then evaluated with the reference measurements from the continuous silicon films

$$\int_{0}^{t_{\rm lith}} i_{\infty}^{\rm rev} dt = \int_{0}^{t_{\rm lith,\infty}} i_{\infty}^{\rm rev} dt = \frac{C_{\infty}^{\rm lith} \left( t_{\rm lith,\infty} \right)}{A_{\rm tot}} - \left\langle i_{\infty}^{\rm irr} \right\rangle t_{\rm lith,\infty}$$
(17)

$$\int_{0}^{t_{\rm linh}} t_{\infty}^{\rm irr} \, \mathrm{d}t = \left\langle i_{\infty}^{\rm irr} \right\rangle t_{\rm lith} \tag{18}$$

The first expression relies on the premise that the reversible specific capacity of the silicon is the same in both patterned and continuous electrodes. However, the irreversible capacity is primarily attributed to lithium loss to the SEI, which is proportional to the surface area and the cycle time. In these expressions, it is important to remember that  $t_{\rm lith}$  is the lithiation time for the patterned film experiment, whereas  $t_{\text{lith},\infty}$  is the lithiation time for the continuous silicon film. Inserting Equations (17) and (18) into Equation (16) and applying an analogous approach for the Cu reference then gives

$$\Delta \kappa_{\rm S}^{\rm lith}\left(t_{\rm lith}\right) = \frac{\left\langle \Delta t_{\rm SLZ}^{\star \, \rm lith} \right\rangle}{\left\langle t_{\rm ior}^{\rm ior} \right\rangle} = \frac{C_{\rm P}^{\rm lith}\left(t_{\rm lith}\right) - \alpha_{\rm o} C_{\rm \infty}^{\rm lith}\left(t_{\rm lith}\right) - (1 - \alpha_{\rm o}) C_{\rm Cu}^{\rm lith}\left(t_{\rm lith}\right)}{\alpha_{\rm o} \alpha_{\rm s}^{\star} A_{\rm tot} t_{\rm lith} \left\langle t_{\rm ior}^{\rm ior} \right\rangle} \quad (19)$$

$$C_{\infty}^{\text{lith}}(t_{\text{lith}}) = C_{\infty}^{\text{lith}}(t_{\text{lith},\infty}) + \langle i_{\infty}^{\text{irr}} \rangle (t_{\text{lith}} - t_{\text{lith},\infty})$$

$$= I_{\infty} t_{\text{lith},\infty} + \langle i_{\infty}^{\text{irr}} \rangle (t_{\text{lith}} - t_{\text{lith},\infty})$$
(20)

$$C_{\text{Cu}}^{\text{lith}}(t_{\text{lith}}) = C_{\text{Cu}}^{\text{lith}}(t_{\text{lith,Cu}}) + \langle i_{\text{Cu}}^{\text{irr}} \rangle (t_{\text{lith}} - t_{\text{lith,Cu}})$$

$$= I_{\text{Cu}} t_{\text{lith,Cu}} + \langle i_{\text{Cu}}^{\text{irr}} \rangle (t_{\text{lith}} - t_{\text{lith,Cu}})$$
(21)

The same general approach can also be used to evaluate the excess (i.e., strain induced) capacity losses in the SLZ during delithiation

$$\Delta \kappa_{\rm S}^{\rm deli}(t_{\rm deli}) = \frac{\left\langle \Delta t_{\rm SLZ}^{*\rm deli} \right\rangle}{\left\langle i_{\infty}^{\rm irr} \right\rangle} = \frac{C_{\rm P}^{\rm deli}(t_{\rm deli}) - \alpha_{\rm o} C_{\infty}^{\rm deli}(t_{\rm deli}) - (1 - \alpha_{\rm o}) C_{\rm Cu}^{\rm deli}(t_{\rm deli})}{\alpha_{\rm o} \alpha_{\rm s}^{*} A_{\rm tot} t_{\rm deli} \left\langle i_{\infty}^{\rm irr} \right\rangle} \tag{22}$$

www.advancedsciencenews.com www.advenergymat.de

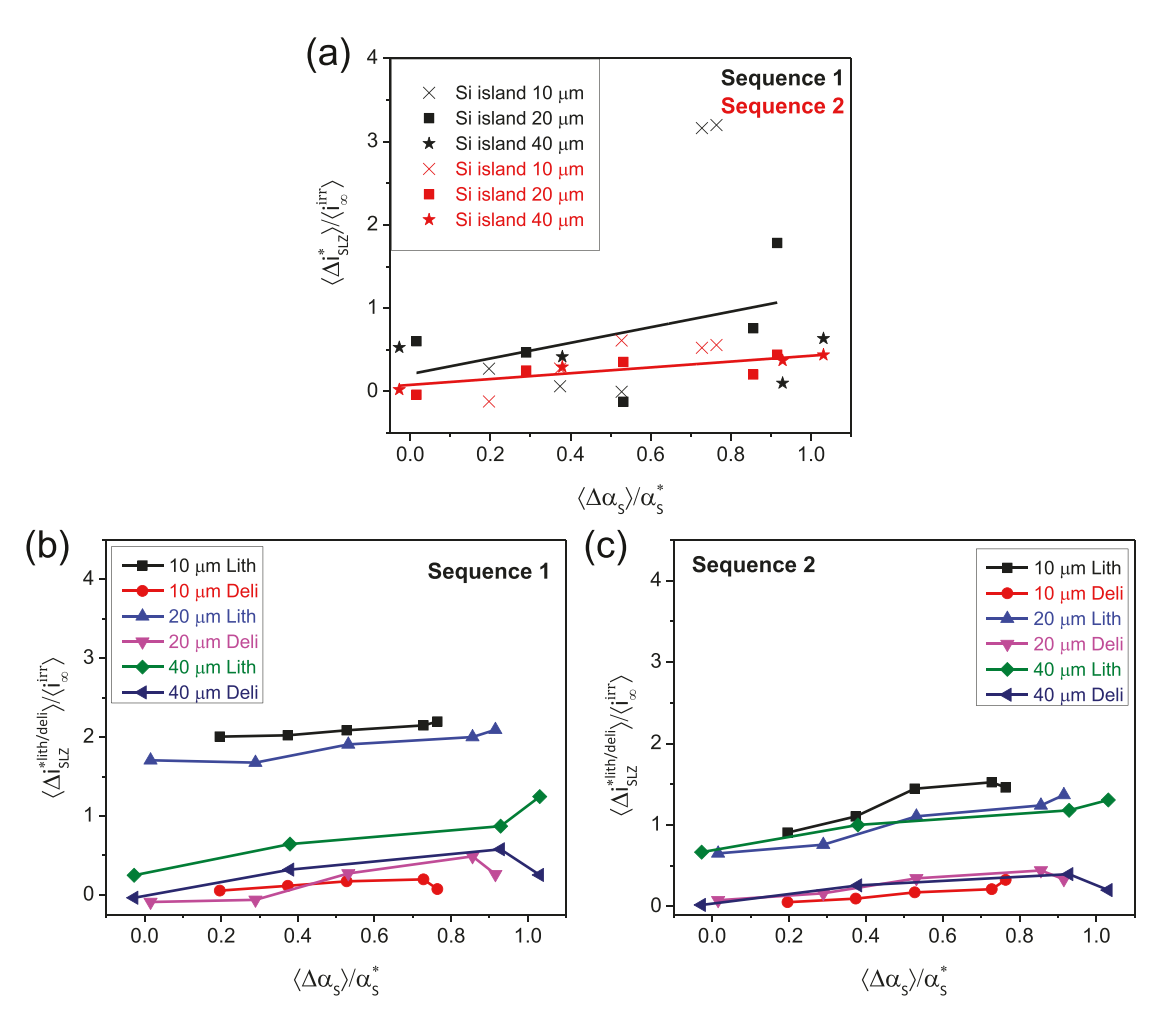


Figure 7. Relative capacity loss due to strain in the shear lag zone, for SEI created with the fast formation cycle (C/2). a) Overall losses, based on applying Equation (11) to the data in Figure 3. The black line is fit to all of the Sequence 1 values (i.e., for different island sizes) and the red line is fit to all of the Sequence 2 values. b) Strain induced losses during lithiation and delithiation for Sequence 1, based on Equations (19) and (22). c) Strain induced losses for Sequence 2.

$$C_{\infty}^{\text{deli}}(t_{\text{deli}}) = C_{\infty}^{\text{deli}}(t_{\text{deli},\infty}) + \langle i_{\infty}^{\text{irr}} \rangle (t_{\text{deli}} - t_{\text{deli},\infty})$$

$$= I_{\infty} t_{\text{deli},\infty} + \langle i_{\infty}^{\text{irr}} \rangle (t_{\text{deli}} - t_{\text{deli},\infty})$$
(23)

$$C_{\text{Cu}}^{\text{deli}}(t_{\text{deli}}) = C_{\text{Cu}}^{\text{deli}}(t_{\text{deli},\text{Cu}}) + \langle i_{\text{Cu}}^{\text{irr}} \rangle (t_{\text{deli}} - t_{\text{deli},\text{Cu}})$$

$$= I_{\text{Cu}} t_{\text{deli},\text{Cu}} + \langle i_{\text{Cu}}^{\text{irr}} \rangle (t_{\text{deli}} - t_{\text{deli},\text{Cu}})$$
(24)

The values of  $\Delta \kappa_s^{\text{lith}}$  and  $\Delta \kappa_s^{\text{deli}}$  for the slow and fast formation cycles are reported in parts (b) and (c) of Figures 6 and 7. These results show that much higher SLZ capacity losses occur during the lithiation cycles, rather than during subsequent delithiation. This occurs for all cycles in both sequences. In contrast, the values for  $\Delta \kappa_s^{\text{deli}}$  indicate that the applied strain has a minimal impact on capacity loss during delithiation. Here, note that  $\Delta \kappa_s^{\text{lith}}$  and  $\Delta \kappa_s^{\text{deli}}$  are calculated relative to the area of the initial silicon in the SLZ. Since Li insertion increases the electrode area in the SLZ, losses that are not affected by strain should lead to  $\Delta \kappa_s^{\text{deli}}$  values that increase proportionally to the area. In other words, an area increase from 0 to 0.2 along the horizontal axis would produce a corresponding increase of 0.2 along the  $\Delta \kappa_s^{\text{deli}}$  axis. The observed increases in  $\Delta \kappa_s^{\text{deli}}$  are

comparable to this relative increase in area. Thus, the capacity losses during delithiation are similar to those measured in the continuous silicon films after normalizing for the area change in the SLZ.

#### 4. Discussion

The schematics in **Figure 8** show proposed explanations for the impact of strain on SEI degradation and subsequent capacity loss. These mechanisms are based on the experimental results in Section 3, along with other relevant information from recent investigations. The following behaviors are depicted:

Large SEI Deformation (Tensile) During Li Insertion: Figure 8a shows basic crack formation that can occur when in-plane tensile strain is applied to the SEI during lithiation of the underlying silicon. This has been observed directly with in situ AFM. [15] In general, the formation of cracks through the SEI will not necessarily lead to excess capacity loss. It has been argued that cracking will enable additional SEI formation by exposing underlying active material to the electrolyte. [33,43,44] However, this requires at least one additional mechanism

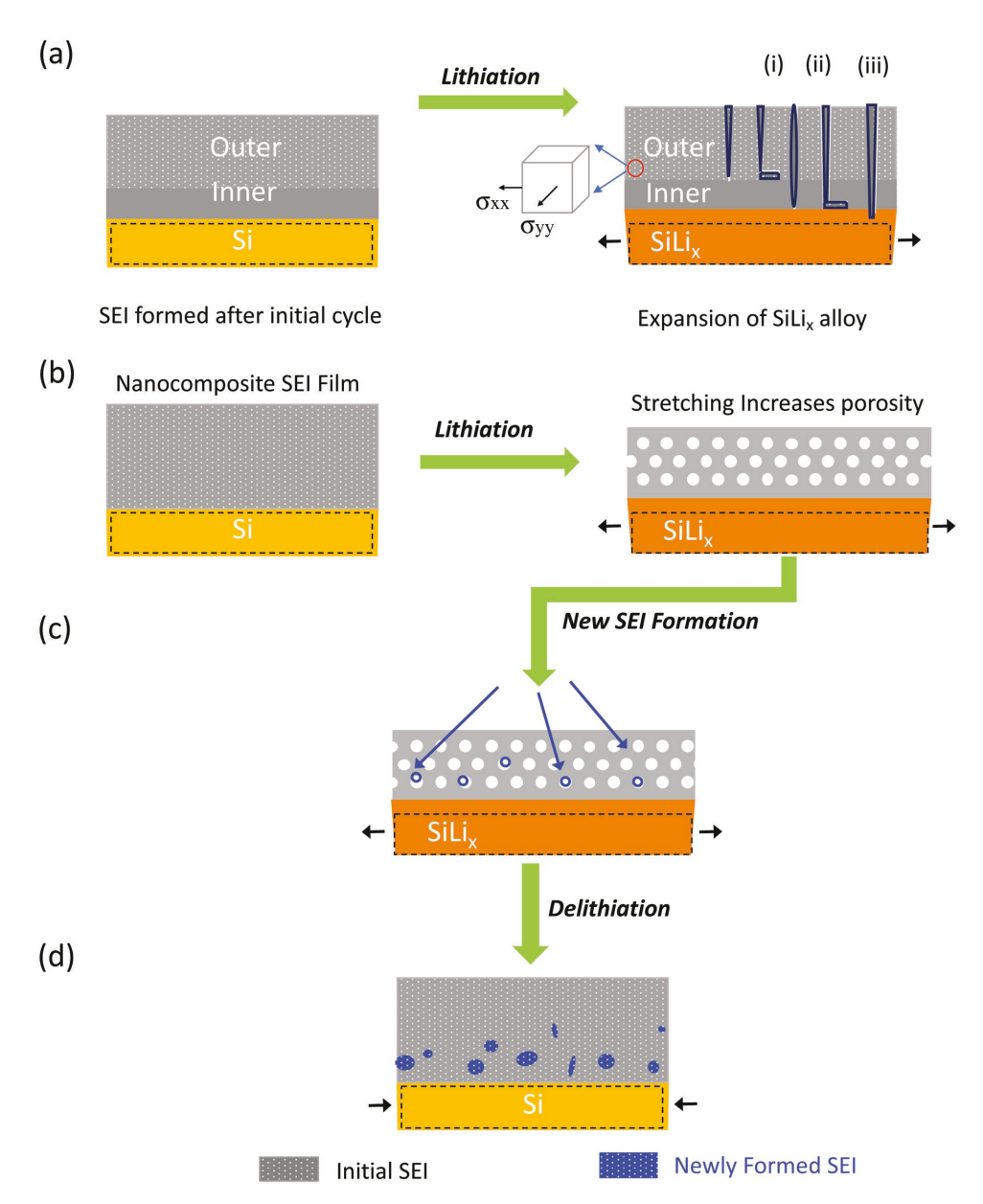


Figure 8. a) Tensile stress in the SEI can induce fracture through the outer layer. Subsequent failure mechanisms that may occur include: (i) crack deflection and debonding between the inner and outer layers, (ii) crack penetration into the inner SEI (with or without crack deflection and debonding at the electrode surface), (iii) crack penetration into the electrode material. For elastic solids the phenomena in Figure 8a are dictated by fracture energies of the film material(s), decohesion energies at the interfaces, and the elastic constants. Based on the large applied strains that occur with silicon electrodes, plastic deformation of the SEI is also likely to be relevant. b) Increased void space inside of the SEI occurs when the expansion of the underlying electrode applies tensile strains to the mesoporous film. c) Reactions at relatively low potentials produce additional by-products inside of the expanded SEI film. d) During delithiation, the contraction of the electrode applies compressive strain to the SEI.

beyond initial crack formation, such as debonding at the electrode/SEI interface or crack penetration into the underlying electrode, which are also shown schematically in Figure 8a.

Internal SEI Formation in Response to Tensile Strain: The conventional failure mechanisms in Figure 8a could certainly contribute to the strain-induced capacity losses during lithiation. However, other recent observations show that cracks in the outer SEI do not necessarily penetrate through the inner SEI, which suggests that there is strong bonding between the SEI layer and the silicon surface. [33,45] This implies that the fracture

and spallation mechanisms in Figure 8a are not necessarily the dominant cause of the strain-induced capacity losses observed in Figures 6 and 7. To understand other ways that large tensile strains can increase lithium losses, it is instructive to consider the internal SEI structure in more detail. It is well documented that SEI consists of both soft organic and harder ceramic phases. A number of reports also indicate that significant mesoporosity is present.<sup>[46–48]</sup> Applying large tensile strains to these nanocomposite thin films should increase this internal porosity. Figure 8b shows a relatively simple way to envision



representation in Figure 8.

www.advenergymat.de

this, via the "sponge-like" stretching of the mesoporous film. The central feature here is that the large applied strains create space inside of the SEI, at length scales that are smaller than those associated with the fracture processes in Figure 8a. With the more open structure in Figure 8b, the Li-consuming side reactions that produce SEI products are likely to be enhanced. This is shown schematically in Figure 8c. Additional experiments are needed to demonstrate that tensile strains can lead to the direct formation of additional constituents inside of the film. This additional electrolyte reduction requires electrons from the underlying Si electrode, which is presumably promoted by mechanical degradation of the inner SEI. It

is difficult to evaluate how this occurs, since the actual mul-

tiphase structure of the SEI is obviously more complex than the

Compressive Strain in SEI During Delithiation: Shrinkage of the silicon-lithium alloy during delithiation will apply compressive strain to the SEI in the SLZ. For a film with a fixed composition that undergoes strictly elastic deformation, one would expect the process to be largely reversible (i.e., the SEI will return to its initial state). However, the formation of additional material inside of the film that is shown in Figure 8c will increase the solid volume that is present, such that a net compressive stress is expected to evolve over the course of each cycle. This is shown schematically in Figure 8d. The results in Figures 6 and 7 indicate that the applied strains here do not result in excess capacity loss during delithiation, which is consistent with the idea that additional SEI formation during the lithiation step changes the SEI structure (i.e., such that there is less capacity loss over the same voltage range during delithiation). However, this improved passivation is lost during the next lithiation cycle, where high capacity losses recur. A likely explanation for this is that mechanical cycling leads to the removal of material from the SEI. At this point it is difficult to ascertain how this material removal occurs. This determination will require additional experiments.

In summary, it is possible that the increases in capacity loss due to tensile strains in the SEI are caused by the mechanisms in Figure 8a that re-expose electrode surfaces to the electrolyte (crack deflection along the electrode/inner SEI interface or crack extension into the electrode). The sequence of mechanisms in Figure 8b-d is also a likely alternative explanation that is consistent with a number of experimental observations. Based on the  $\Delta \kappa_{\rm S}^{\rm lith}$  and  $\Delta \kappa_{\rm S}^{\rm deli}$  values in Figures 6 and 7, it is logical to conclude that the SEI structure must be different during lithiation and delithiation (note that the different exposure time during the two portions of the cycle are accounted for by the analysis that leads to the current densities  $\langle \Delta i_{\rm SLZ}^{* \, lith} \rangle$  and  $\langle \Delta i_{\rm SLZ}^{* \, deli} \rangle$ ). Because the SEI "sees" the same range of voltages during the lithiation and delithiation steps, the large difference between  $\Delta\kappa_{\rm S}^{
m lith}$  and  $\Delta\kappa_{\rm S}^{
m deli}$  indicates that changes that occur during lithiation lead to changes in the SEI structure that significantly reduce capacity loss during delithiation. Comparing the  $\Delta \kappa_s^{\text{lith}}$ and  $\Delta \kappa_{\rm S}^{\rm deli}$  values in Sequence 1 with those in Sequence 2 shows that there is some reduction in capacity loss over time. However, the basic trend of large  $\Delta \kappa_s^{lith}$  and small  $\Delta \kappa_s^{deli}$  is repeated in every cycle. This indicates that changes during each step that lead to the much lower  $\Delta \kappa_S^{deli}$  value are largely (but not completely) reversed during the subsequent cycle, where relatively large  $\Delta \kappa_s^{\text{lith}}$  values are again observed during lithiation.

The impact that the initial SEI formation cycle has on the results in Figures 6 and 7 can also be interpreted in terms of the proposed mechanisms in Figure 8. With the faster formation cycle, the reduction in the strain-induced capacity losses is primarily observed during the lithiation portion of each cycle, where the  $\Delta \kappa_{\rm S}^{\rm lith}$  values in Figure 7 are noticeably lower than those in Figure 6 (but still much larger than the unstrained reference case). In both cases the impact of strain on  $\Delta \kappa_s^{\text{deli}}$  is relatively small. Thinner films are generally less susceptible to the failure modes in Figure 8a, and thus the lower straininduced capacity losses that occur after the fast formation cycle are generally consistent with the thinner SEI that forms under these conditions. It is also reasonable that the phenomena in Figure 8b-d will lead to more capacity loss with thicker SEI films. Here, we propose that thinner films are likely to be more fatigue resistant during repeated cycling. Mechanical degradation related to the nanoscale, multiphase structure of these films can lead to the loss of material which then reforms in later cycles. It is likely that these small scale failure mechanisms inside of the SEI films were not detected in our prior in situ AFM experiments. It is also possible that the internal SEI formation might be catalyzed by the existing film material, so that internal reactions will lead to larger losses when the existing film is thicker.

The interpretations outlined above are also consistent with the minimal impact of the low voltage hold during the fast formation cycle (i.e., the observation that the results in Figure 4e,f are quantitatively similar to those in Figure 4c,d). Prior work indicates that the initial SEI thickness is primarily established by the organic decomposition reactions that occur at higher potentials.<sup>[10]</sup> It appears that the inorganic phases that form inside of the SEI then passivate the surface relatively quickly at low potentials. Once this passivation layer is in place, the low voltage hold does not produce a significant amount of additional SEI (i.e., because the surface is already passivated). This is consistent with both the similar capacity losses and the similar SEI thickness with and without the low voltage hold. While this long hold during the formation cycle has minimal impact, the large strains that are applied to the SEI film during subsequent cycling then lead to the degradation of the passivation properties provided by this inorganic material. However, these degradation mechanisms are not impacted by the long potentiostatic hold during the formation cycle, which supports the idea that this hold does not substantially change the SEI structure.

# 5. Conclusion

The research presented here measures the impact of SEI strain on irreversible lithium losses. These quantitative values cannot be obtained with other existing methods. This method is based on the idea that the SLZ in small Si islands can be used to apply large, controlled strains to SEI films. By comparing results with multiple island sizes and using appropriate unstrained reference films, it is possible to quantify the excess capacity loss due to strain. The analysis that was employed compares the data sets with different island sizes, where the relative contributions

www.advenergymat.de

displacement, u(r), for an axisymmetric radial expansion, using the

from the SLZ increase with decreasing island size. The same characteristic length scale describes the size of the SLZ, and a value for this quantity (\$\hat{s}^\*\$) was obtained from self-consistent fitting of the data sets with an appropriate analytical model. This analysis also made it possible to separate the contributions that occur during the lithiation and delithiation portions of an electrochemical cycle.

To demonstrate this capability, three different formation cycles were investigated. In all of these cases, there were large strain-induced capacity losses due to the applied tensile strain in the SEI during lithiation (i.e., when the silicon was expanding). During delithiation, the impact of strain on capacity losses was almost non-existent (within the accuracy limits inherent in the measurements and the analysis employed). Also, varying the formation cycle significantly altered the magnitude of the measured strain-induced losses during lithiation. Here, when the SEI was formed slowly (C/20 first cycle), the average straininduced capacity enhancement for full cycles (to 0.05 V) was more than a factor of 2 higher than it was for SEI that was formed at a much faster rate (C/2). This difference was still apparent after 14 subsequent cycles.

# 6. Experimental Section

Thin film specimens were prepared by electron-beam evaporation at a rate of 0.1 nm s<sup>-1</sup>. A 300 nm thick copper film was first deposited on steel disc substrates (0.5 mm thick, 16 mm diameter). Amorphous silicon was then deposited on top of the copper. Patterned silicon islands were produced by depositing films through custom brass masks (0.005 in. thick, with 10, 20, or 40  $\mu m$  holes separated by twice the hole spacing). Continuous silicon films were also deposited without masks, as reference samples. All of the silicon films were grown to thicknesses of 50 nm, which are thin enough to prevent cracking and delamination during electrochemical cycling. All three types of films (continuous copper, continuous silicon, and patterned silicon) were placed in CR-2032 coin cells that were assembled in an Ar-filled glove box, where Li foil was both the counter and reference electrode. The electrolyte was a mixed solution of 1 M LiPF6 in ethylene carbonate and ethyl methyl carbonate (3:7 volume ratio, Gotion, USA).

Galvanostatic discharge/charge tests were performed with a Bio-Logic VSP potentiostat in the voltage window of 0.05-1.5 V (vs Li+/Li). EIS measurements were conducted from 10 mHz to 100 kHz, at the end of the voltage holds. After these tests, the coin cells were disassembled in the glove box and the silicon electrodes were examined with scanning electron microscopy (FIB, FEI HELIOS 600).

For each of the SEI formation conditions described in Section 2, a total of 21 samples were tested (three each of seven different types). Average capacities during lithiation and delithiation were measured for three continuous silicon films. For the different patterned silicon island sizes, the surface area for the silicon and exposed copper varies. Because of this difference, continuous copper reference films were run at a different current density for each island size. Thus, to obtain the necessary data, three patterned silicon and three continuous copper samples were tested for each silicon island size ( $6 \times 3$  total).

# **Appendix**

#### **Elastic Analysis**

The previously published elastic analysis of circular silicon islands provides a starting point for evaluating the experimental results in Section 2. This treatment is based on evaluating the in-plane

$$\frac{d}{dr} \left[ \frac{1}{r} \frac{d(ru)}{dr} \right] + b = 0 \tag{A1}$$

following differential equation

where b accounts for the body force acting in the radial direction. The in-plane displacements are then obtained by solving this with appropriate boundary conditions.

For the inner region  $(0 \le r \le R_P)$ , b = 0 and u (0) = u  $(R_P) = 0$ . The solution is then u(r) = 0, which leads to biaxial compressive strain in the film, with no in-plane strain applied to the SEI. In the outer region  $(R_P \le r \le R)$ , Equation (A1) is solved with

$$b = \frac{\tau_s}{h} \frac{1 - \nu_f^2}{E_F} \tag{A2}$$

along with the boundary conditions:  $u(R_p) = 0$  and  $\sigma_{rr}(R) = 0$ . At a given state of charge (i.e., value of  $\chi$ ), the expanded size of the island is related to the displacement via

$$R(\chi) = R_o + u(R,\chi) \tag{A3}$$

The solution of Equation (A1) then gives the following relationships:

$$B = \left(3\frac{\hat{s}}{R} - 2 - \nu_f\right) + \sqrt{9\left(\frac{\hat{s}}{R}\right)^2 - 6(2 + \nu_f)\frac{\hat{s}}{R} + \frac{(5 + 3\nu_f)}{(1 - \nu_f)}}$$
(A4)

$$\frac{R_{\rm p}}{R} = \frac{\left(1 + \nu_{\rm f}\right)}{B^{1/3} \left(1 - \nu_{\rm f}\right)^{2/3}} - \left(\frac{B}{1 - \nu_{\rm f}}\right)^{\frac{1}{3}} \tag{A5}$$

where the key parameter, \$, varies with lithiation according to

$$\hat{s} = -\frac{\sigma_{e}^{\odot}h}{\tau_{s}} = -\frac{E_{f}}{1 - \nu_{f}} \varepsilon^{\infty} \frac{h_{o}}{\tau_{s}} (1 - 2 \nu_{f} \varepsilon^{\infty}) \cong \frac{E_{f}}{1 - \nu_{f}} \frac{h_{o}}{\tau_{s}} \frac{V_{i,j} \chi}{3V_{o}^{\odot}}$$
(A6)

For an island with a given initial size and thickness ( $R_o$  and  $h_o$ ), Equations (A4)–(A6) can be solved to obtain  $R_p$  and R (and also B) if  $\hat{s}$  is specified. Reasonable values for the elastic constants and molar volumes in Equation (A7) can be obtained from the literature. Thus,  $\tau_s$  is the key unknown quantity here. Obtaining this value from the experiments is discussed further in Section 3.2.

Physically, the value of \$\hat{s}\$ in Equation (A6) provides an approximate measure of the size of the shear lag zone, S. Much of the data analysis methodology in section 3 relies on this similarity. From Equation (A5)

$$\frac{S}{R} = \frac{R - R_p}{R} = 1 - \frac{(1 + \nu_f)}{B^{1/3} (1 - \nu_f)^{2/3}} + \left(\frac{B}{1 - \nu_f}\right)^{1/3}$$
(A7)

Based on the relatively small value of  $\chi^*$  in Equation (3), most of the lithiation (and delithiation) process occurs under conditions where plastic deformation of the silicon must be considered. These changes can be evaluated with finite element modeling (FEM), however, it is impractical to use detailed FEM to fit the electrochemical data from a large number of experiments. Thus, we developed an approximate analytical approach that describes deformation after the inner region reaches  $\sigma_f^*$ . This treatment employs the following simplifying assumptions: 1) the Li induced volume changes are isotropic and fully reversible, with constant  $V_{Li}$ ; 2) uniform lithiation occurs through the film thickness (i.e., Li diffusion in the Si is fast); 3) initial stress in the Si

To evaluate  $R(\chi)$  for  $\chi > \chi^*$ , the island is divided into three regimes. After the onset of plastic flow in the inner region  $(0 \le r \le R_P^*)$ , uniform thickness changes continue as  $\chi$  varies. The undeformed thickness here is

$$h_{\infty} = h_{\rm o} \left( 1 + f_{\rm z}^{\infty} \right) \tag{A8}$$

www.advenergymat.de

ADVANCED ENERGY MATERIALS

The out-of-plane expansion strain,  $f_z^{\infty}$ , can be described in terms of f by noting that the total volume here is  $\pi(R_P^*)^2 h_o V(\chi)$ , and invoking Equations (1) and (2) to obtain

$$(1+f_z^{\infty}) = \frac{(1+f)^3}{(1-\varepsilon_{\infty}^{\infty})^2}$$
 (A9)

The SLZ at any point in time corresponds to  $R_P(t) \le r \le R(t)$ . If the deformation here is treated as fully elastic, the undeformed thickness is given by

$$h(r) = h_o(1+f) \tag{A10}$$

Between the inner region and the SLZ, there is also a transition region  $(R_p^* \le r \le R_p(t))$ . Here, at a given point, the material is initially in the SLZ (i.e., at  $\chi^{\pm}$ ), however, plastic flow begins to occur as expansion occurs and  $R_p$  increases. For our approximate analysis, the undeformed thickness in this transition region is estimated with a simple linear interpolation

$$h(r) \cong h_o \left[ \left( 1 + f_z^{\infty} \right) + \left( f - f_z^{\infty} \right) \frac{\left( r - R_p^{\ast} \right)}{\left( R_p(t) - R_p^{\ast} \right)} \right]$$
(A11)

The full volume of the island can then be described by summing the contributions from the three regions outlined above

$$V(\chi) \cong \frac{V_n^{o}}{R_0^2 h_o} \left[ \left[ R_p^* \left( 1 - \varepsilon_{el}^{\infty} \right) \right]^2 h_o \left( 1 + f_z^{\infty} \right) + R_o^2 \alpha_S h_o \left( 1 + f \right) + h_o \left( 1 + f_z^{\infty} \right) \left( 1 - \varepsilon_{el}^{\infty} \right)^2 \int_{R_r^c}^{R_r} 2r \frac{h(r)}{h_o \left( 1 + f_z^{\infty} \right)} dr \right]$$
(A12)

To evaluate the integral for the transition region, inserting Equation (A11) gives

$$\int_{R_{p}^{*}}^{R_{p}} 2r \left[ 1 - \frac{\left( f_{z}^{\infty} - f \right) \left( r - R_{p}^{*} \right)}{\left( 1 + f_{z}^{\infty} \right) \left( R_{p} - R_{p}^{*} \right)} \right] dr = \left( R_{p}^{*} \right)^{2} \int_{1}^{p} 2\hat{p} \left[ 1 - \varphi \frac{\left( \hat{p} - 1 \right)}{\left( p - 1 \right)} \right] d\hat{p}$$
 (A13)

$$\varphi = \frac{(f_z^{\infty} - f)}{(1 + f_z^{\infty})}; \hat{p} = \frac{r}{R_p^{\infty}}; p = \frac{R_p}{R_p^{\infty}}$$
(A14)

Integration and substituting Equation (A13) then gives the following revised form of Equation (A12):

$$V(\chi) \cong V_{m}^{o} (1 + f_{z}^{\infty})$$

$$\left( \left[ \frac{R_{p}^{*}}{R_{o}} \right]^{2} + \frac{\alpha_{S} (1 + f)}{(1 + f_{z}^{\infty})} + \left[ \frac{R_{p}^{*}}{R_{o}} \right]^{2} \left[ (p^{2} - 1) - \frac{2\varphi}{(p - 1)} \left( \frac{(p^{3} - 1)}{3} - \frac{(p^{2} - 1)}{2} \right) \right] \right)$$
(A15)

This simplifies to:

$$\frac{\left(1+f\right)^{3}}{\left(1+f_{z}^{\infty}\right)\left(1-\varepsilon_{pl}^{\infty}\right)^{2}}=1=\frac{\alpha_{S}}{\left(1+f\right)^{2}}+\left(\frac{R_{p}^{*}}{R_{o}}\right)^{2}\left[1+\left[\left(p^{2}-1\right)-\frac{\varphi}{3}\left(2p^{2}-p-1\right)\right]\right] \tag{A16}$$

Inserting the definition of  $\alpha_S$  (Equation 4) and noting that  $R_P^* \cong R_o - S^*$  then gives

$$\frac{2S^*R_o - S^{*2}}{\left(R_o - S^*\right)^2} - \frac{S^2}{\left(R_o - S^*\right)^2 \left(1 + f\right)^2} = \frac{2S}{\left(R_o - S^*\right) \left(1 + f\right)^2} p + \left[\left(p^2 - 1\right) - \frac{\varphi}{3} \left(2p^2 - p - 1\right)\right]$$
(A17)

This quadratic can then be readily solved for p(f).

# **Supporting Information**

Supporting Information is available from the Wiley Online Library or from the author.

# Acknowledgements

The authors thank Dr. H. Kim (SK Innovation, Korea), Dr. R. Kumar (Lam Research), and Dr. X. Xiao (General Motors) for fruitful discussions. This work was supported by SK Innovation. Additional support was also provided by the Assistant Secretary for Energy Efficiency and Renewable Energy, Vehicle Technologies Office of the U.S. Department of Energy under Contract No. Award Number DE-EE0007787 under the Battery Material Research (BMR) Program.

#### **Conflict of Interest**

The authors declare no conflict of interest.

## Keywords

capacity loss, lithium-ion battery, SEI formation, shear lag zone

Received: October 2, 2018 Revised: November 8, 2018 Published online: December 13, 2018

- [1] E. Peled, J. Electrochem. Soc. 1979, 126, 2047.
- [2] J. Li, J. R. Dahn, J. Electrochem. Soc. 2007, 154, A156.
- [3] B. Philippe, R. Dedryvère, M. Gorgoi, H. Rensmo, D. Gonbeau, K. Edström, Chem. Mater. 2013, 25, 394.
- [4] L. Y. Beaulieu, T. D. Hatchard, A. Bonakdarpour, M. D. Fleischauer, J. R. Dahn, J. Electrochem. Soc. 2003, 150, A1457.
- [5] M. Nie, D. P. Abraham, Y. Chen, A. Bose, B. L. Lucht, J. Phys. Chem. C 2013, 117, 13403.
- [6] A. L. Michan, M. Leskes, C. P. Grey, Chem. Mater. 2016, 28, 385.
- [7] J. P. Maranchi, A. F. Hepp, A. G. Evans, N. T. Nuhfer, P. N. Kumta, J. Electrochem. Soc. 2006, 153, A1246.
- [8] C. Cao, H. G. Steinrück, B. Shyam, K. H. Stone, M. F. Toney, *Nano Lett.* 2016, 16, 7394.
- [9] V. Etacheri, R. Marom, R. Elazari, G. Salitra, D. Aurbach, Energy Environ. Sci. 2011, 4, 3243.
- [10] A. Tokranov, B. W. Sheldon, C. Li, S. Minne, X. Xiao, ACS Appl. Mater. Interfaces 2014, 6, 6672.
- [11] A. Cresce, S. M. Russell, D. R. Baker, K. J. Gaskell, K. Xu, Nano Lett. 2014, 14, 1405.
- [12] Y. Horowitz, H. G. Steinrück, H. L. Han, C. Cao, I. I. Abate, Y. Tsao, M. F. Toney, G. A. Somorjai, *Nano Lett.* 2018, 18, 2105.
- [13] J. Vetter, P. Novák, M. R. Wagner, C. Veit, K. C. Möller, J. O. Besenhard, M. Winter, M. Wohlfahrt-Mehrens, C. Vogler, A. Hammouche, J. Power Sources 2005, 147, 269.
- [14] P. Lu, C. Li, E. W. Schneider, S. J. Harris, J. Phys. Chem. C 2014, 118, 896.
- [15] P. Verma, P. Maire, P. Novák, Electrochim. Acta 2010, 55, 6332.
- [16] J. B. Goodenough, K. S. Park, J. Am. Chem. Soc. 2013, 135, 1167.
- [17] U. Kasavajjula, C. Wang, A. J. Appleby, J. Power Sources 2007, 163, 1003.
- [18] S. F. Lux, I. T. Lucas, E. Pollak, S. Passerini, M. Winter, R. Kostecki, Electrochem. Commun. 2012, 14, 47.
- [19] M. B. Pinson, M. Z. Bazant, J. Electrochem. Soc. 2013, 160, A243.
- [20] E. Peled, S. Menkin, J. Electrochem. Soc. 2017, 164, A1703.
- [21] Y. Jin, S. Li, A. Kushima, X. Zheng, Y. Sun, J. Xie, J. Sun, W. Xue, G. Zhou, J. Wu, F. Shi, Energy Environ. Sci. 2017, 10, 580.
- [22] Y. Horowitz, H. L. Han, F. A. Soto, W. T. Ralston, P. B. Balbuena, G. A. Somorjai, *Nano Lett.* **2018**, *18*, 1145.
- [23] C. Sämann, K. Kelesiadou, S. S. Hosseinioun, M. Wachtler, J. R. Köhler, K. P. Birke, M. B. Schubert, J. H. Werner, Adv. Energy Mater. 2018, 8, 1701705.



www.advancedsciencenews.com www.advenergymat.de

ADVANCED ENERGY MATERIALS

- [24] H. Wu, G. Chan, J. W. Choi, I. Ryu, Y. Yao, M. T. McDowell, S. W. Lee, A. Jackson, Y. Yang, L. Hu, Y. Cui, Nat. Nanotechnol. 2012, 7, 310.
- [25] F. Shi, Z. Song, P. N. Ross, G. A. Somorjai, R. O. Ritchie, K. Komvopoulos, *Nat. Commun.* 2016, 7, 11886.
- [26] A. Casimir, H. Zhang, O. Ogoke, J. C. Amine, J. Lu, G. Wu, Nano Energy 2016, 27, 359.
- [27] L. David, R. Bhandavat, U. Barrera, G. Singh, Nat. Commun. 2016, 7, 10998.
- [28] S. Chen, L. Shen, P. A. van Aken, J. Maier, Y. Yu, *Adv. Mater.* **2017**, 29, 1605650.
- [29] S. Choi, T. W. Kwon, A. Coskun, J. W. Choi, Science 2017, 357, 279.
- [30] T. W. Kwon, J. W. Choi, A. Coskun, Chem. Soc. Rev. 2018, 47, 2145.
- [31] J. Zheng, H. Zheng, R. Wang, L. Ben, W. Lu, L. Chen, L. Chen, H. Li, Phys. Chem. Chem. Phys. 2014, 16, 13229.
- [32] R. Kumar, P. Lu, X. Xiao, Z. Huang, B. W. Sheldon, ACS Appl. Mater. Interfaces 2017, 9, 28406.
- [33] R. Kumar, A. Tokranov, B. W. Sheldon, X. Xiao, Z. Huang, C. Li, T. Mueller, ACS Energy Lett. 2016, 1, 689.
- [34] J. Graetz, C. Ahn, R. Yazami, B. Fultz, Electrochem. Solid-State Lett. 2003, 6, A194.
- [35] J. R. Szczech, S. Jin, Energy Environ. Sci. 2011, 4, 56.

- [36] S. Pal, S. S. Damle, S. H. Patel, M. K. Datta, P. N. Kumta, S. Maiti, J. Power Sources 2014, 246, 149.
- [37] Y. He, X. Yu, Y. Wang, H. Li, X. Huang, Adv. Mater. 2011, 23, 4938.
- [38] M. T. McDowell, S. W. Lee, J. T. Harris, B. A. Korgel, C. Wang, W. D. Nix, Y. Cui, *Nano Lett.* 2013, 13, 758.
- [39] A. Tokranov, R. Kumar, C. Li, S. Minne, X. Xiao, B. W. Sheldon, Adv. Energy Mater. 2016, 6, 1502302.
- [40] H. Haftbaradaran, S. K. Soni, B. W. Sheldon, X. Xiao, H. Gao, J. Appl. Mech. 2012, 79, 031018.
- [41] S. K. Soni, B. W. Sheldon, X. Xiao, A. Tokranov, Scr. Mater. 2011, 64,
- [42] V. B. Shenoy, P. Johari, Y. Qi, J. Power Sources 2010, 195, 6825.
- [43] D. Aurbach, J. Power Sources 2000, 89, 206.
- [44] N. Liu, H. Wu, M. T. McDowell, Y. Yao, C. Wang, Y. Cui, Nano Lett. 2012, 12, 3315.
- [45] R. Kumar, Ph.D. Degree Thesis, Brown University, 2017.
- [46] F. Single, B. Horstmann, A. Latz, J. Electrochem. Soc. 2017, 164, F3132
- [47] U. S. Vogl, S. F. Lux, E. J. Crumlin, Z. Liu, L. Terborg, M. Winter, R. Kostecki, J. Electrochem. Soc. 2015, 162, A603.
- [48] M. Sina, J. Alvarado, H. Shobukawa, C. Alexander, V. Manichev, L. Feldman, T. Gustafsson, K. J. Stevenson, Y. S. Meng, Adv. Mater. Interfaces 2016, 3, 1600438.